minerals

MDPI

Article

Monazite U-Pb Chronology, Pyrite Rb-Sr Chronology and Isotope Geochemistry of the Xidouya Gold Deposit in the Jiaodong Peninsula, Eastern China: Constraints on the Timing and Process of Mineralization

Faqiang Zhao [1,2,3], Zhimin Li [2,3], Peng Guo [2,3], Tongliang Tian [2,3], Bin Li [2,3], Jiabin Yu [2,3], Dongyue Li [2,3], Pengpeng Zhang [4] and Jiepeng Tian [5,6,*]

1 College of Earth Science and Engineering, Shandong University of Science and Technology, Qingdao 266590, China
2 Shandong Institute of Geophysical and Geochemical Exploration, Jinan 250013, China
3 Shandong Engineering Research Center of Underground Resources and Environment High Precision Detection, Jinan 250013, China
4 Institute of Geophysical and Geochemical Exploration, Chinese Academy of Geological Science, Langfang 065000, China
5 Key Laboratory of Building Structural Retrofitting and Underground Space Engineering, Ministry of Education, Jinan 250101, China
6 School of Civil Engineering, Shandong Jianzhu University, Jinan 250101, China
* Correspondence: tianjiepeng20@sdjzu.edu.cn

Abstract

The Jiaodong gold concentration area, one of the most important gold metallogenic belts in China, has long been the focus of contentious debates regarding the genetic mechanisms and timing of gold mineralization. This study presents the new monazite U-Pb and pyrite Rb-Sr isotopic chronology data for the No. I ore zone of the Xidouya gold deposit, integrated with H-O-S isotopic geochemical analyses, to systematically investigate the mineralization age, ore-forming fluid sources and material provenance of the deposit. The main mineralization age of the deposit is constrained to 117 Ma, which is highly consistent with the regional mineralization peak of 120 ± 5 Ma in the Jiaodong gold concentration area. The δD values of the fluids range from −88.0‰ to −75.0‰ (mean = −82.6‰), while the $\delta^{18}O_{H_2O}$ values are calculated to be between 4.6‰ and 6.1‰. H-O isotopic data indicate that the ore-forming fluids of the Xidouya gold deposit originated from a mixed magmatic and meteoric source. As mineralization progressed from Stage I through Stage III, there was a detectable trend of increasing meteoric water involvement and a general decrease in δD and $\delta^{18}O_{H_2O}$ values. This signature indicates that the initial mineralizing system was dominated by primary magmatic water which subsequently underwent significant water–rock interaction with Early Cretaceous granitic bodies and progressive dilution by meteoric fluids in an open tectonic environment. Furthermore, sulfur isotopes (average $\delta^{34}S$ = +7.43‰) and the initial strontium isotope ratio ($^{87}Sr/^{86}Sr$ = 0.71012) support a mixed-source model for the ore-forming materials, likely dominated by the anatexis of ancient crust with potential minor mantle-derived contributions. During the Early Cretaceous, lithospheric thinning and extension in the North China Craton (NCC) triggered large-scale magmatism and mineralization. The Xidouya gold deposit is a direct product of these regional tectono-magmatic-mineralizing events. This study provides new high-precision isotopic dating data for the Xidouya gold deposit, clarifies the evolutionary history of ore-forming fluids and the supply mechanism of ore-forming materials, and provides important theoretical insights and practical references for gold prospecting and exploration in the eastern part of the Jiaodong gold concentration area.

Check for updates

Received: 15 February 2026
Revised: 14 March 2026
Accepted: 19 March 2026
Published: 23 March 2026

Copyright: © 2026 by the authors. Licensee MDPI, Basel, Switzerland. This article is an open access article distributed under the terms and conditions of the Creative Commons Attribution (CC BY) license.

Keywords: Xidouya gold deposit; monazite U-Pb dating; pyrite Rb-Sr dating; H-O-S isotopes; ore-forming material source

1. Introduction

The Jiaodong gold concentration area represents a major gold resource base in China with favorable metallogenic conditions, hosting proven gold resources of 5800 t [1–4]. It can be further subdivided into three concentration areas from west to east: the Jiaoxibei (Zhaoyuan–Laizhou), Qipengfu (Qixia–Penglai–Fushan) and Muru (Muping–Rushan) gold concentration areas [5,6]. The large to super-large gold deposits are predominantly distributed in the Jiaoxibei gold concentration area, whereas the Qipengfu gold concentration area is dominated by small and medium-sized gold deposits [7]. The Xidouya gold deposit investigated in this study is located in the Qipengfu gold concentration area, with proven gold reserves of 11.56 t [8]. As one of the few gold deposits with reserves exceeding 10 t in this concentration area, it is adjacent to the Hushan gold deposit with reserves of nearly 20 t [7]. The discovery of these two medium-to-large gold deposits demonstrates the significant metallogenic potential of this region. In-depth research on the Xidouya gold deposit not only serves as a key supplement to the gold metallogenic patterns of the Qipengfu gold concentration area but also challenges the traditional perception that only small and medium-sized deposits are present in this area. The mineralized concentration area formed by the Xidouya and Hushan gold deposits provides a typical case for analyzing the ore-controlling structures, mineralization age, ore-forming fluid evolution and gold enrichment mechanisms of the Qipengfu gold concentration area, and the research findings will also offer important theoretical and practical guidance for gold prospecting and exploration in the eastern part of the entire Jiaodong gold concentration area.

In recent years, the controlling effects of Mesozoic granites on gold mineralization have attracted extensive attention from geoscientists worldwide. Similarly, the role of the lithospheric mantle in regulating gold mineralization has also become a major research focus. Some researchers propose that metasomatism of the convective mantle or subducted slab materials and their overlying sediments may lead to the anomalous enrichment of gold and volatiles in the mantle, which could represent the source of ore-forming fluids and materials for gold deposits in the Jiaodong gold concentration area [9–11]. Other researchers argue that the ore-forming materials of gold deposits were derived from the metasomatically enriched lithospheric mantle during subduction events, with the incorporation of crustal components during migration [12–14]. A consensus has been reached that the main phase of gold mineralization in the Jiaodong gold concentration area occurred at 120 ± 5 Ma [15–18]. Some studies suggest a west-to-east younging trend of mineralization ages across the province [19,20].

Previous studies have been conducted on the geological characteristics, deep prospecting potential, and implications of fluid inclusions for ore-forming fluid evolution of the Xidouya gold deposit, yielding preliminary understandings [7,21–24]. Some researchers have proposed that the Xidouya gold deposit is an epigenetic mesothermal-to-epithermal hydrothermal-altered cataclastic rock-type deposit with favorable prospecting potential in the deep and peripheral areas [22]. Others suggest that the No. I orebody of the Xidouya gold deposit is contiguous with that of the Hushan gold deposit, belonging to a single deposit with total gold reserves reaching 30 t (a large gold deposit) [7]. Additionally, studies on the No. II orebody of the Xidouya gold deposit indicate that the ore-forming fluids are dominated by mixed magmatic and meteoric water, characterized by mesothermal to epithermal temperatures, moderate to low salinity and low density, with a mineralization

depth ranging from 5.81 to 7.82 km [23]. However, the aforementioned studies are relatively limited in investigating the relationship between Mesozoic tectono-magmatic activities and gold mineralization, as well as the source of ore-forming materials and the precise mineralization age. The genetic type of the gold deposit and the tectonic dynamic setting of mineralization remain unclear.

The widely developed quartz–pyrite–polymetallic sulfide gold ores in the Xidouya gold deposit provide a new opportunity to elucidate the timing and genesis of gold mineralization. As the most common gold-bearing sulfide in gold deposits, pyrite is a direct recorder of fluid activity and material migration during mineralization [17]. U-Pb isotope analysis was conducted on monazite separated from the gold-bearing quartz–pyrite veins within the main ore body of the Xidouya gold deposit, combined with Rb-Sr isotope analysis of pyrite, to precisely constrain the mineralization age of the deposit. Based on detailed geological evidence and petrographic characteristics, the newly obtained isotopic chronology data are interpreted as the precise mineralization age of the Xidouya gold deposit. Using the H-O-S isotopic compositions, we reconstruct the physico-chemical conditions of mineralization, clarify the origin and evolutionary process of ore-forming fluids, identify the end-members of ore-forming material supply, and discuss the deposit genesis, thereby providing key geochemical evidence for summarizing regional metallogenic regularity and guiding gold prospecting and exploration.

2. Regional Geological Setting

The Jiaodong gold concentration area is tectonically located at the southeastern margin of the North China Craton (NCC), consisting of the Jiaobei Uplift in the north, the Jiaolai Basin in the central part and the Jiaodong Terrane in the southeast (Figure 1a) [25–28]. The Jiaobei Uplift and the Jiaodong Terrane are bounded by the Muping–Jimo Fault, which also constitutes the suture zone between the North China Craton and the Yangtze Craton [26,27]. The Qipengfu gold concentration area is situated within the Jiaobei Uplift, where the metamorphic basement is well developed, mainly comprising the Neoarchean tonalite–trondhjemite–granodiorite (TTG) gneiss suite with Triassic ultra-high-pressure metamorphic rocks (UHP gneiss) [29]. The exposed strata include the Neoarchean biotite leptynite, plagioclase amphibolite, hornblende leptynite intercalated with magnetite quartzite assemblage, Paleoproterozoic meta-sedimentary rocks, Neoproterozoic slate and sandstone, Early Cretaceous volcanic sedimentary rocks, and Quaternary sediments (Figure 1b) [30]. Mesozoic intrusive rocks are extensively developed, mainly including the Late Jurassic granites (Linglong granite) and Early Cretaceous granites (Guojialing granite, Weideshan granite and Yushan granodiorite porphyry) [6]. In addition, various dykes such as Mesozoic lamprophyre, diabase and quartz diorite dykes are widely distributed throughout the area.

The Jiaodong gold concentration area is characterized by well-developed ductile shear zones and brittle fault structures. Ductile shear zones are mainly exposed in the ancient metamorphic basement; the Archean Qixia granite–greenstone belt is featured by widespread striped and banded structures in rocks, accompanied by numerous small folds of various morphologies, with elongated “school-of-fish” mafic rock inclusions visible within the zones [31]. Brittle fault structures are dominated by NNE- and NE-trending faults, which are closely associated with gold mineralization, with scattered EW-, NW- and SN-trending faults interspersed among them (Figure 1b). These brittle faults and their associated secondary and tertiary fault systems provide essential channels and reservoir spaces for the migration, enrichment and precipitation of ore-bearing hydrothermal fluids.

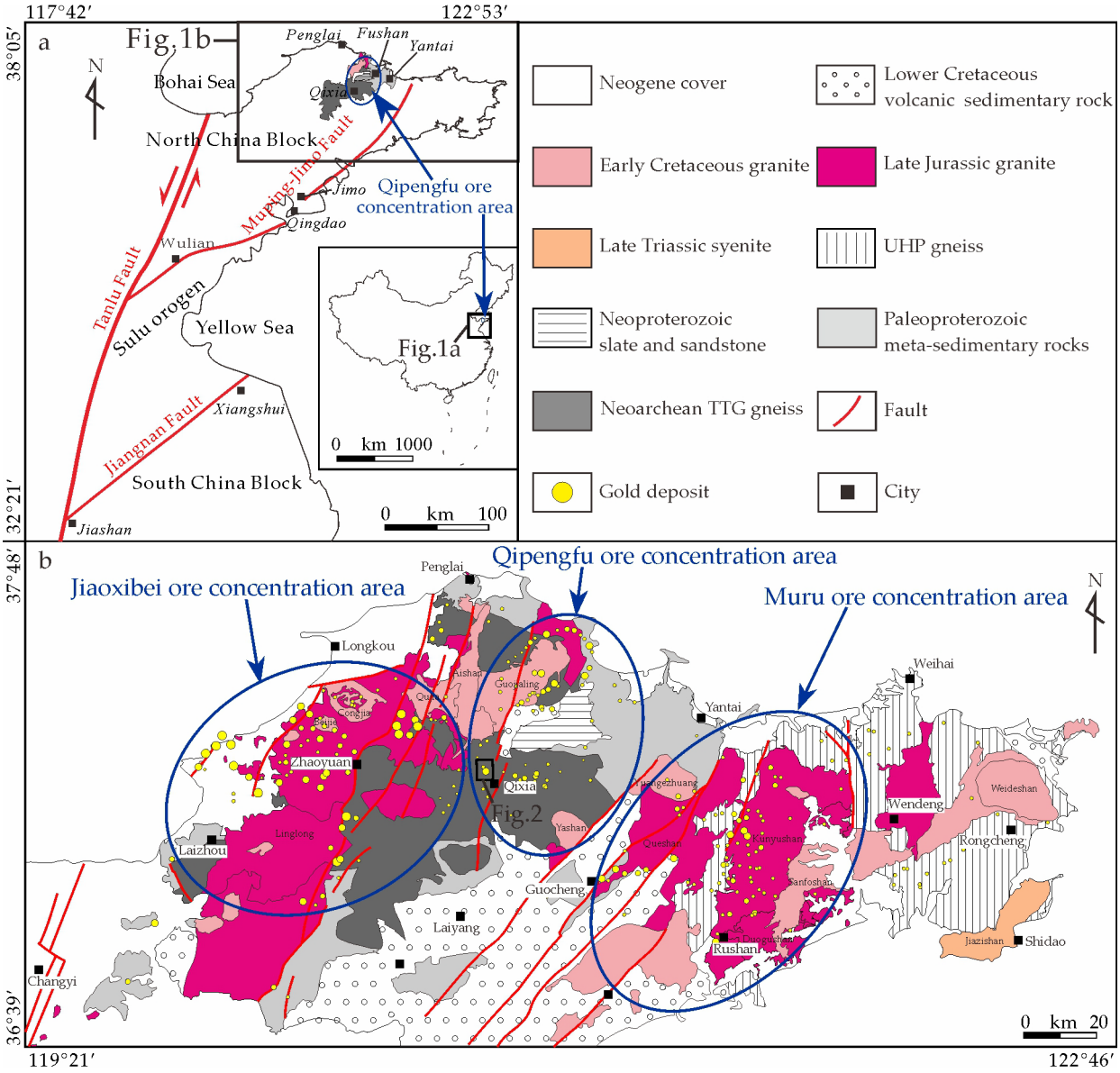


Figure 1. Regional distribution and simplified geological map of the Jiaodong Peninsula (modified after [25,32]). (**a**) The tectonic division for the Jiaodong Peninsula between the North China Craton and the Sulu orogen along the Tan–Lu Fault. (**b**) Simplified geology in the Jiaodong Peninsula.

3. Ore Deposit Geology

The stratigraphy in the study area is relatively simple. The basement lithology of the mining area is primarily composed of Paleoproterozoic metamorphic strata, which are dominated by fine-grained biotite leptynite with local enclaves of tremolite-feldspar-quartzite (Figure 2a). In addition, Quaternary sediments, such as sandy clay and conglomerate, are distributed across the surface of the mining area. The surface-exposed magmatic rocks mainly include Meso-Neoarchean gneissic hornblende–trondhjemitic gneiss and fine-grained hornblende trondhjemite, Early Neoarchean plagioclase amphibolite, Late Jurassic porphyritic medium-coarse grained monzogranite, and the dykes are mainly Late Yanshanian quartz diorite dykes (Figure 2) [22].

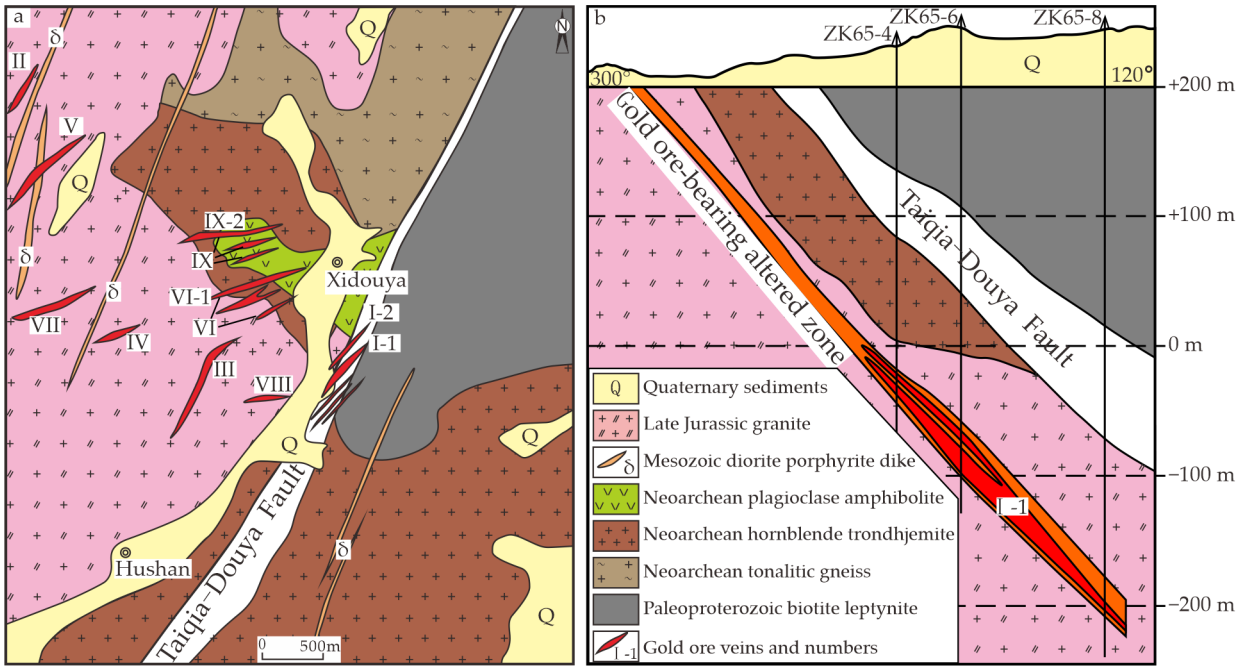


Figure 2. Geological map of the Xidouya gold deposit (**a**) and the exploration profile of line 65 (**b**) (modified after [23]).

The NE-trending Taiqian–Douya Fault Zone runs through the entire study area and represents the first-order fault in the mining area. The fault has a total length of 36 km, with a strike of approximately 30–40°, dipping southeast at an angle of 28–35° and a length of about 3 km within the study area [22]. The fault is mostly developed near the contact zones of different rock masses and exhibits distinct polyphase activity characteristics. Early-stage activity formed mylonite and cataclasite; middle-stage activity was characterized by extensional (transtensional) features with breccias of various sizes; late-stage activity transformed into a transpressional fault with extensive grayish-white cataclasite and mylonite developed [23]. Disseminated and veinlet pyritization can be observed in the deep part of the fault. NNE-trending secondary faults developed in groups in the footwall of this fault, and several faults with roughly parallel strikes and close spacing form a composite fault zone. All ore-bearing altered zones in the area are strictly controlled by the above types of faults.

Orebodies are mainly located in the footwall of the Taiqian–Douya Fault Zone, with their occurrence and scale strictly controlled by the fault system, and the host rocks are mainly porphyritic medium–coarse-grained monzogranite. There are seven industrially valuable orebodies in the deposit, represented by No. I, VI and IX orebodies [22]. This study selects the No. I orebody for a detailed description, which can be further divided into the No. I-1 main orebody and the No. I-2 minor orebody. The No. I-1 orebody occurs as vein and lenticular shapes, with a strike of 23–29°, dipping southeast at an angle of 25–30° (Figure 2b). It extends about 700 m along the strike and 450 m along the dip, with a thickness ranging from 0.87 to 25 m and an average thickness of approximately 5.12 m. The gold grade varies from 1.12 ppm to 13.31 ppm, with an average grade of 3.28 ppm and a maximum grade of 13.31 ppm in a single sample [21]. The No. I-2 orebody is lenticular and vein-shaped, with a strike of 20–36°, dipping southeast at an angle of 28–30°. It stretches about 485 m along the strike and 350 m along the dip, with a thickness of 1.0–6.3 m (average 1.34 m) and a gold grade of 1.74–4.02 ppm (average 2.85 ppm) [21].

The ores exhibit a variety of textures, dominated by crystalline granular, metasomatic relict, interstitial and euhedral–subhedral textures. The ore structures are mainly dissem-

inated and brecciated structures. The mineral composition is relatively simple; metallic minerals are mainly native gold and pyrite, with minor pentlandite, pyrrhotite and chalcopyrite (Figure 3). Gangue minerals are mainly quartz, sericite and carbonate minerals. Native gold occurs mainly as angular grains, followed by elliptical grains, and is primarily hosted in the interior of pyrite grains and intergranular fractures of pyrite, with a grain size generally less than 50 μm (Figure 3). Hydrothermal alteration types mainly include pyritization, potassic alteration, propylitization (including zoisitization, epidotization and clinozoisitization), sericitization, silicification and carbonatization.

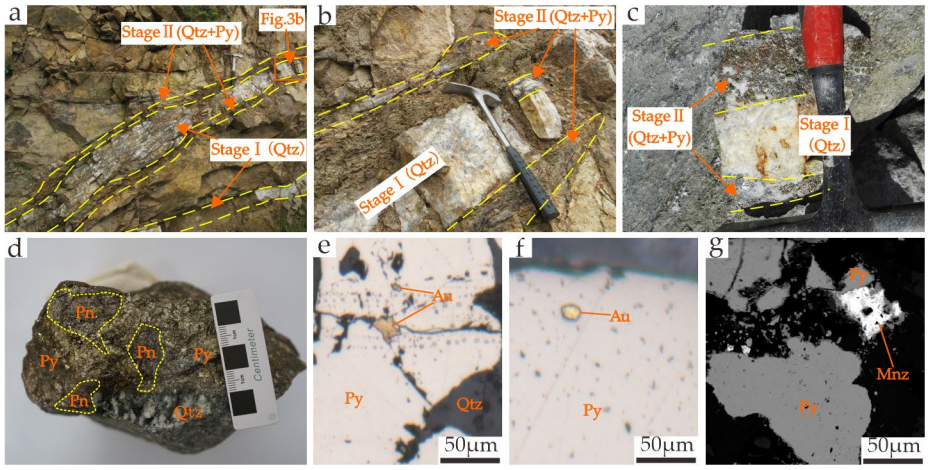


Figure 3. Representative photographs of outcrops and photomicrographs of samples from the Xidouya gold deposit. (**a**–**c**) Field outcrop photographs showing the spatial relationship between two stages of mineralized veins. Stage I (Qtz) consists of early-stage milky quartz veins, which occur as banded bodies, are relatively pure, and contain well-developed microfractures. Stage II (Qtz + Py) quartz–pyrite polymetallic sulfide veins developed along both sides of Stage I veins, exhibiting a bedding-parallel relationship. (**d**) Hand specimen photograph of pyrite-bearing polymetallic sulfide ore, with a mineral assemblage of quartz, pyrite, and pentlandite. (**e**) Photomicrograph (reflected light) showing native gold occurring as granular particles in the intercrystalline spaces or fractures of pyrite, with quartz present as a gangue mineral. (**f**) Photomicrograph (reflected light) showing native gold occurring as fine inclusions within pyrite. (**g**) Assemblage of monazite and pyrite. Abbreviations: Qtz: Quartz; Au: Gold; Py: Pyrite; Pn: Pentlandite; Mnz: Monazite.

Based on mineral paragenetic associations and cross-cutting relationships, the mineralization process of the deposit is divided into three distinct stages: I, Au–quartz–pyrite stage; II, Au–quartz–polymetallic sulfide stage (the main mineralization stage); III, quartz-carbonate stage [22].

4. Sampling and Analytical Methods

Samples for experimental analysis were collected from the No. I ore zone of the Xidouya gold deposit at a depth of −100 to −105 m, including ore types of quartz–pyrite and quartz–polymetallic sulfide. Polished sections were prepared for ore microscopic and petrographic observations, and some samples were completely ground to separate single minerals, followed by mount preparation and photography. H-O-S isotopic analyses were conducted at the Key Laboratory of Metallogenic Processes and Resource Assessment, Ministry of Natural Resources, Institute of Mineral Resources, Chinese Academy of Geological Sciences, Beijing, China. Isotopic chronology analyses were all completed at the Isotopic Chronology Laboratory, Tianjin Center, as part of the China Geological Survey, Tianjin, China.

4.1. H-O Isotope Analysis

Quartz from each mineralization stage was selected for H-O isotopic analysis. Samples were crushed to 40–60 mesh, and pure quartz single minerals (purity > 99%) were carefully hand-picked under a binocular microscope. Analyses were performed on a MAT-251EM mass spectrometer (Finnigan MAT GmbH, Bremen, Germany), with an analytical precision of ±0.2‰relative to the Vienna Standard Mean Ocean Water (V-SMOW) standard. δD values were determined by the Zn reduction method for hydrogen production: water was extracted from fluid inclusions in quartz by the vacuum thermal decrepitation method, and the extracted water reacted with high-purity Zn at 400 °C to generate H_2 for mass spectrometric analysis [33]. $\delta^{18}O$ values were measured by the BrF_5 equilibration method: quartz single minerals reacted with BrF_5 at 450–550 °C for nearly 2 h to produce oxygen, and pure oxygen was obtained by separating impurities such as SiF_4 and BrF_3 using a combined cold trap. The purified oxygen reacted with carbon rods step by step at 700 °C under platinum catalysis, and the generated CO_2 gas was collected sequentially for mass spectrometric analysis [34].

4.2. S Isotope Analysis

Fresh and pure pyrite single minerals (purity > 99%) were hand-picked after crushing the ore samples. Sulfide samples were oxidized to SO_2 with Cu_2O as the oxidant under high-vacuum conditions at 1000 °C for 15 min, and the generated SO_2 was used for sulfur isotope analysis. The analysis was carried out on a MAT-251EM mass spectrometer relative to the Vienna Canyon Diablo Troilite standard, with an analytical precision of ±0.2‰.

4.3. Monazite U-Pb Dating

Monazite single minerals were separated from quartz-pyritized ores of the mineralization Stage II. Backscattered electron (BSE) images of monazite were obtained at the Experimental Testing Laboratory, Tianjin Center, China Geological Survey. U-Pb isotopic dating was performed using a New Wave 193 nm laser ablation system coupled with a Thermo Fisher Neptune (Thermo Fisher Scientific, Bremen, Germany) multi-collector inductively coupled plasma mass spectrometer (MC-ICP-MS). The laser spot diameter for monazite analysis was 25 μm, with a pulse frequency of 5 Hz and a laser energy density of 10–11 J/cm^2. The monazite standard 44069 (pale-yellow euhedral equigranular monazite from the Wilmington Complex, Delaware, USA) was used for external calibration. Detailed experimental procedures refer to previous studies [35,36]. Data processing was conducted using the ICPMSData program [37], and weighted mean age calculation and concordia diagram plotting were completed with the Isoplot program [38,39]. Experimental analytical errors were reported at the 1σ level.

4.4. Pyrite Rb-Sr Dating

Rb-Sr isotopic analysis was also separated from quartz-pyritized ores of the mineralization Stage II, with a total of eight samples selected for analysis. To ensure the isotopic signature accurately reflected the primary ore-forming fluid and to eliminate potential contamination from late-stage carbonate veins or secondary inclusions, the pyrite grains were subjected to rigorous ultrasonic cleaning and a sequential acid-leaching procedure prior to dissolution. Following this purification step, appropriate amounts of the pyrite samples were accurately weighed and dissolved using a mixed acid solution of HNO_3 and $HClO_4$. The dissolved sample solution was evenly divided into two parts: one part was spiked with an appropriate amount of ^{87}Rb + ^{84}Sr mixed diluent, and after chemical separation and purification, it was used for the determination of Rb and Sr content; the other part was used for the determination of Sr isotopic ratios after separation and purifi-

cation. The Rb and Sr separation procedure adopted the traditional AG50W × 12 cation exchange resin separation process, with gradient elution using HCl solutions of different concentrations to collect Rb and Sr fractions separately. Rb and Sr isotopic analyses were performed on a TRITON thermal ionization mass spectrometer (TIMS, manufactured by Thermo Fisher Scientific, Bremen, Germany). Specific experimental separation procedures and instrumental test parameters refer to previous studies [40] and isochron age calculation was completed with the Isoplot program [38,39].

5. Results

5.1. H-O Isotopic Compositions of Quartz

A total of nine sets of H-O isotopic data were obtained in this study, combined with three sets of previously published data (Table 1). The δD values range from −88.0‰ to −75.0‰ with an average of −82.6‰, and the $\delta^{18}O$ values vary from 10.3‰ to 12.2‰ with a mean of 11.2‰. The hydrogen isotopic composition of the ore-forming fluid is consistent with that of water in quartz fluid inclusions, and the oxygen isotopic composition of the fluid was calculated based on the oxygen isotopic composition of quartz and the mineralization temperature of different stages. To calculate the oxygen isotopic composition of the fluid ($\delta^{18}O_{H_2O}$), the maximum homogenization temperature of the fluid inclusions at each stage was used. Because the homogenization temperatures generally represent the lower limit of the actual mineralization temperature, and our studied system lacks clear evidence of fluid boiling, applying the maximum homogenization temperature provides the most reasonable approximation to the true trapping conditions during mineralization. Previously measured homogenization temperatures of fluid inclusions for stages I, II and III of the No. I ore zone in the Xidouya gold deposit are 323 °C, 336 °C, and 353 °C, respectively [24]. Based on the oxygen isotope fractionation equation between quartz and water, "$1000\ln_\alpha{}^{Q-W} = 3.38 \times 10^6/T^2 - 2.90$" [41], the oxygen isotope composition $\delta^{18}O_{H_2O}$ of water in the mineralizing hydrothermal fluid is estimated as follows: $\delta^{18}O_{H_2O} = \delta^{18}O_{SMOW} - 1000\ln_\alpha{}^{Q-W}$.

Table 1. Hydrogen and oxygen isotope compositions in the Xidouya gold deposit.

Stage	Mineral	δD_{smow} (‰)	$\delta^{18}O_{smow}$ (‰)	$\delta^{18}O_{H_2O}$ (‰)	$T_{h\text{-}TOT}$ (°C)	Source
I	Quartz	−77.0	12.0	5.9	323	This study
	Quartz	−81.0	11.8	5.7	323	
	Quartz	−75.0	12.2	6.1	323	
II	Quartz	−82.0	11.5	5.8	336	This study
	Quartz	−84.0	11.2	5.5	336	
	Quartz	−79.0	11.0	5.3	336	
	Quartz	−81.0	10.8	5.1	336	[23]
	Quartz	−86.0	10.4	4.7	336	
	Quartz	−86.0	10.3	4.6	336	
III	Quartz	−87.0	10.9	5.7	353	This study
	Quartz	−85.0	11.1	5.9	353	
	Quartz	−88.0	10.6	5.4	353	

In terms of different mineralization stages, the fluid in Stage I has δD values of −81.0‰ to −75.0‰ (average −77.7‰, $n = 3$), $\delta^{18}O$ values of 11.8‰ to 12.2‰ (average 12.0‰), and $\delta^{18}O_{H_2O}$ values of 5.7‰ to 6.1‰ (average 5.9‰). The fluid in Stage II exhibits δD values

of −86.0‰ to −79.0‰ (average −83.0‰, n = 6), $\delta^{18}O$ values of 10.3‰ to 11.5‰ (average 10.9‰), and $\delta^{18}O_{H_2O}$ values of 4.6‰ to 5.8‰ (average 5.2‰). The fluid in Stage III has δD values of −88.0‰ to −85.0‰ (average −86.7‰, n = 3), $\delta^{18}O$ values of 10.6‰ to 11.1‰ (average 10.9‰), and $\delta^{18}O_{H_2O}$ values of 5.4‰ to 5.9‰ (average 5.6‰).

5.2. S Isotopic Compositions

S isotopic studies were mainly conducted for Stage I and II of mineralization, with a total of 14 sets of new S isotopic data obtained and 22 sets of previously published data collected, amounting to 36 sets of data in total (Table 2). The $\delta^{34}S$ values show a narrow range of variation from 5.82‰ to 8.63‰ with an average of +7.43‰, all positively deviated from meteoritic sulfur ($\delta^{34}S$ = 0‰) (Figure 4). By stages, the $\delta^{34}S$ values of pyrite in the ore-forming fluid of Stage I range from 7.51‰ to 8.63‰ with an average of 8.13‰. In Stage II, the $\delta^{34}S$ values of pyrite in the ore-forming fluid vary from 5.93‰ to 8.22‰ (average 7.44‰), and the $\delta^{34}S$ values of chalcopyrite range from 5.82‰ to 6.85‰ (average 6.30‰).

Table 2. Sulfur isotopic analyses in the Xidouya gold deposit.

Stage	Sample Number	Mineral	$\delta^{34}S_{V\text{-}CDT}$ (‰)	Source	Stage	Sample Number	Mineral	$\delta^{34}S_{V\text{-}CDT}$ (‰)	Source
I	XDY1-1	Pyrite	8.28	This study	II	SD17-11B1-5	Pyrite	7.26	[23]
	XDY1-2	Pyrite	8.15			SD17-11B1-6	Pyrite	7.30	
	XDY1-3	Pyrite	8.01			SD17-11B1-7	Pyrite	7.60	
	XDY1-4	Pyrite	8.36			SD17-11B1-8	Pyrite	7.70	
	XDY1-5	Pyrite	7.83			SD17-11B1-9	Pyrite	7.50	
	XDY1-6	Pyrite	8.25			SD17-11B1-10	Pyrite	7.30	
	XDY1-7	Pyrite	7.51			SD17-12 B1-1	Pyrite	7.70	
	XDY1-8	Pyrite	8.63			SD17-12 B1-2	Pyrite	7.90	
II	XDY3-1	Pyrite	8.22			SD17-12B1-3	Pyrite	6.91	
	XDY3-2	Pyrite	8.20			SD17-12B1-4	Pyrite	7.74	
	XDY3-3	Pyrite	7.73			SD17-12B1-5	Pyrite	7.78	
	XDY3-4	Pyrite	7.27			SD17-12B1-6	Pyrite	6.21	
	XDY3-5	Pyrite	8.05			SD17-12B1-11	Pyrite	5.93	
	XDY3-6	Pyrite	8.10			SD17-11B1-12	Chalcopyrite	6.85	

Table 2. *Cont.*

Stage	Sample Number	Mineral	$\delta^{34}S_{V\text{-}CDT}$ (‰)	Source	Stage	Sample Number	Mineral	$\delta^{34}S_{V\text{-}CDT}$ (‰)	Source
II	SD17-11B1-1	Pyrite	6.94	[23]	II	SD17-11B1-13	Chalcopyrite	5.82	[23]
	SD17-11B1-2	Pyrite	7.40			SD17-11B1-14	Chalcopyrite	6.04	
	SD17-11B1-3	Pyrite	7.13			SD17-11B1-15	Chalcopyrite	6.59	
	SD17-11B1-4	Pyrite	7.16			SD17-11B1-16	Chalcopyrite	6.19	

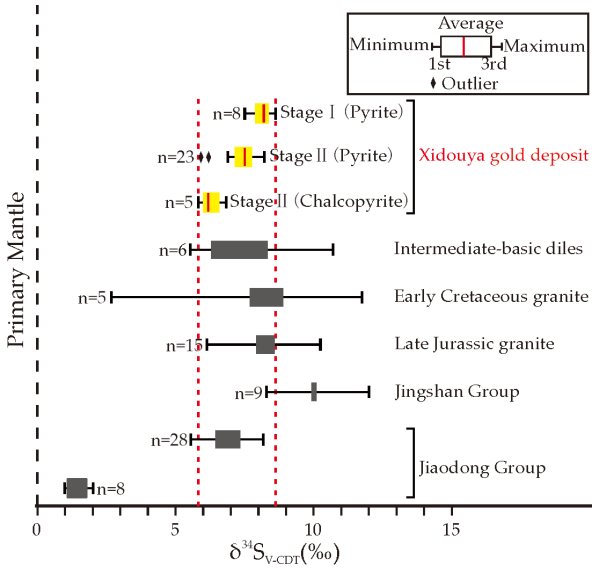


Figure 4. The sulfur isotope compositions of pyrite from the Xidouya gold deposit as well as those from other geological units in Jiaodong. The Intermediate–basic Diles complex $\delta^{34}S$ data from [42]. The Early Cretaceous granitic complex $\delta^{34}S$ data from [43]. The Late Jurassic granitic complex $\delta^{34}S$ data from [43,44]. The Jingshan group $\delta^{34}S$ data from [45]. The Jiaodong group $\delta^{34}S$ data from [43,46–48].

5.3. Monazite U-Pb Ages

Monazite grains recovered from the Stage II quartz–pyrite veins are dark gray and exhibit euhedral to subhedral morphologies, with grain sizes typically ranging from 50 to 100 μm (Figure 5). Th content is an effective geochemical indicator for distinguishing monazite genetic types: hydrothermal monazite typically has low U and Th content, with highly variable Th/U ratios in low-temperature metamorphic and hydrothermal monazite; high-grade metamorphic and magmatic monazite have high Th contents, usually greater than 3% [49,50]. Backscattered electron (BSE) imaging reveals that these grains possess a homogeneous internal texture and lack obvious compositional zoning—features that are consistent with a hydrothermal rather than a magmatic or high-grade metamorphic origin (Figure 5). Furthermore, the maximum Th content is approximately 2.3%, which provides additional support for a hydrothermal genesis (Table 3). Notably, two monazite grains yielded older $^{206}Pb/^{238}U$ ages of 132.7 Ma and 123.4 Ma (Table 3). Based on their distinct textural positioning and older isotopic signatures, these grains are interpreted as inherited relicts derived from the host wall-rock; consequently, they were excluded from the final age calculation. The remaining 26 analyses plot on or closely along the concordia line, yielding a weighted mean $^{206}Pb/^{238}U$ age of 116.69 ± 1.2 Ma (MSWD = 2.4)

(Figure 6). Given their paragenetic association with the primary sulfide minerals and their geochemical characteristics, this date is interpreted to represent the timing of the syn-ore hydrothermal event.

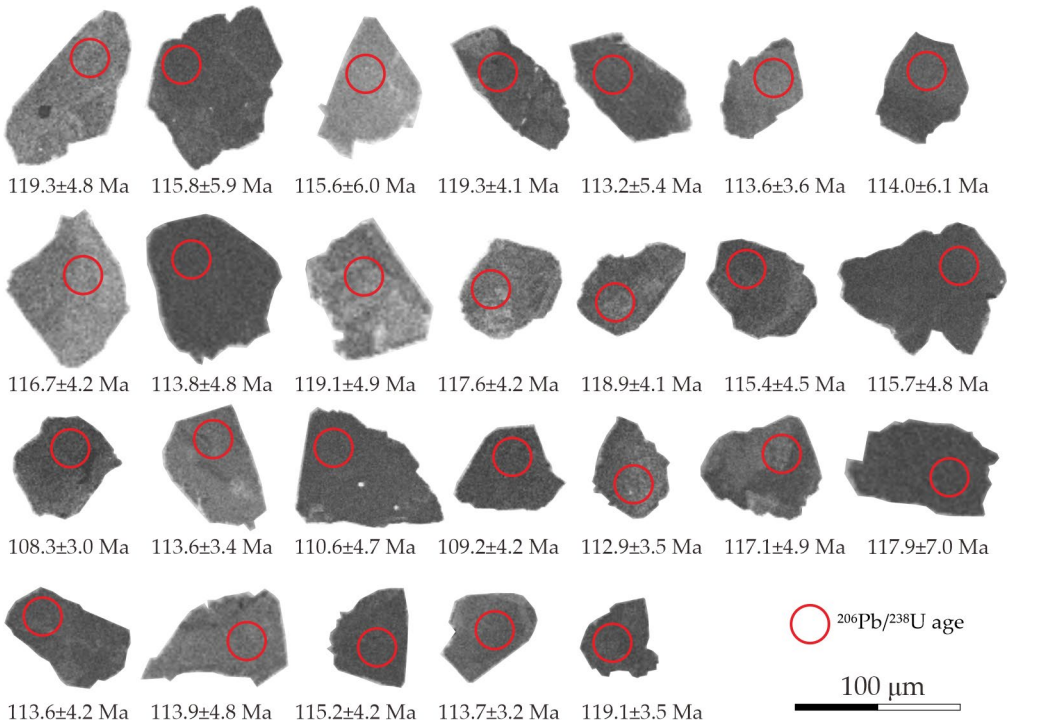


Figure 5. Backscattered images of Monazites from the pyrite–quartz vein in the Xidouya gold deposit.

Table 3. Monazite LA-ICP-MS U-Pb data for spot analysis.

Sample Number	Pb (ppm)	Th (ppm)	U (ppm)	$^{206}Pb/^{238}U$	1σ	$^{207}Pb/^{235}U$	1σ	$^{208}Pb/^{232}Th$	1σ	$^{232}Th/^{238}U$	1σ	$^{206}Pb/^{238}U$	1σ	$^{207}Pb/^{235}U$	1σ
XDY5B1.1	25	23,069	1101	0.0170	0.0002	0.1285	0.0042	0.0051	0.0002	20.7112	0.0265	115.8	5.9	121.8	3.0
XDY5B1.2	21	17,030	945	0.0175	0.0003	0.1290	0.0046	0.0052	0.0001	17.7686	0.0117	119.3	4.8	122.2	3.4
XDY5B1.3	3	2974	150	0.0169	0.0003	0.1268	0.0059	0.0053	0.0002	18.2458	0.0157	115.6	6.0	120.2	4.7
XDY5B1.4	12	12,473	480	0.0175	0.0003	0.1342	0.0055	0.0054	0.0002	25.3075	0.0271	119.3	4.1	126.8	4.2
XDY5B1.5	15	15,883	713	0.0166	0.0002	0.1232	0.0047	0.0046	0.0001	21.8846	0.0112	113.2	5.4	116.9	3.5
XDY5B1.6	7	6920	317	0.0166	0.0003	0.1293	0.0062	0.0051	0.0002	20.9832	0.0076	113.6	3.6	122.5	4.9
XDY5B1.7	2	2646	123	0.0171	0.0003	0.1232	0.0072	0.0049	0.0002	19.4328	0.0076	116.7	4.2	117.0	5.9
XDY5B1.8	1	2009	87	0.0175	0.0004	0.1338	0.0084	0.0053	0.0002	20.0557	0.0079	119.1	4.9	126.5	7.0
XDY5B1.9	9	9249	426	0.0167	0.0003	0.1249	0.0054	0.0050	0.0002	21.0453	0.0078	114.0	6.1	118.5	4.2
XDY5B1.10	7	6888	351	0.0173	0.0003	0.1266	0.0060	0.0051	0.0002	18.9185	0.0081	117.6	4.2	120.0	4.8
XDY5B1.11	9	8596	458	0.0167	0.0003	0.1224	0.0048	0.0046	0.0001	18.2640	0.0106	113.8	4.8	116.2	3.6
XDY5B1.12	7	7667	284	0.0175	0.0003	0.1261	0.0054	0.0054	0.0001	25.8584	0.0286	118.9	4.1	119.6	4.2
XDY5B1.13	14	13,742	686	0.0163	0.0002	0.1165	0.0044	0.0047	0.0001	19.6631	0.0075	115.4	4.5	110.9	3.2
XDY5B1.14	11	9322	543	0.0170	0.0003	0.1208	0.0047	0.0048	0.0001	16.7614	0.0060	115.7	4.8	114.8	3.5
XDY5B1.15	7	6865	377	0.0158	0.0003	0.1131	0.0062	0.0046	0.0002	17.6123	0.0127	108.3	3.0	107.8	5.0
XDY5B1.16	4	6199	169	0.0166	0.0003	0.1250	0.0072	0.0044	0.0001	34.1488	0.0256	113.6	3.4	118.6	5.9
XDY5B1.17	6	6283	322	0.0162	0.0003	0.1227	0.0061	0.0045	0.0002	18.7300	0.0079	110.6	4.7	116.5	4.8
XDY5B1.18	3	4308	179	0.0159	0.0003	0.1232	0.0073	0.0046	0.0001	22.4590	0.0081	109.2	4.2	117.0	6.0
XDY5B1.19	7	7657	368	0.0165	0.0003	0.1230	0.0053	0.0047	0.0001	20.1011	0.0113	112.9	3.5	116.8	4.1
XDY5B1.20	4	3475	220	0.0172	0.0003	0.1305	0.0067	0.0052	0.0002	14.9187	0.0160	117.1	4.9	123.5	5.4
XDY5B1.21	24	19,481	934	0.0197	0.0003	0.1448	0.0049	0.0058	0.0002	20.5805	0.0101	132.7	5.9	136.3	3.6
XDY5B1.22	8	7594	401	0.0173	0.0003	0.1289	0.0055	0.0049	0.0002	18.3310	0.0106	117.9	7.0	122.1	4.2
XDY5B1.23	5	5483	271	0.0166	0.0003	0.1279	0.0062	0.0045	0.0002	19.3355	0.0088	113.6	4.2	121.2	4.9
XDY5B1.24	6	4590	324	0.0167	0.0003	0.1278	0.0055	0.0046	0.0001	13.6059	0.0099	113.9	4.8	121.1	4.2
XDY5B1.25	4	4937	205	0.0182	0.0003	0.1382	0.0061	0.0051	0.0002	22.6653	0.0094	123.4	3.6	130.4	4.8
XDY5B1.26	9	8658	437	0.0169	0.0003	0.1291	0.0054	0.0049	0.0001	19.2556	0.0180	115.2	4.2	122.3	4.1
XDY5B1.27	5	4892	275	0.0166	0.0003	0.1184	0.0057	0.0048	0.0002	17.0044	0.0050	113.7	3.2	112.7	4.5
XDY5B1.28	7	6139	344	0.0175	0.0003	0.1346	0.0061	0.0051	0.0002	17.2002	0.0187	119.1	3.5	127.2	4.8

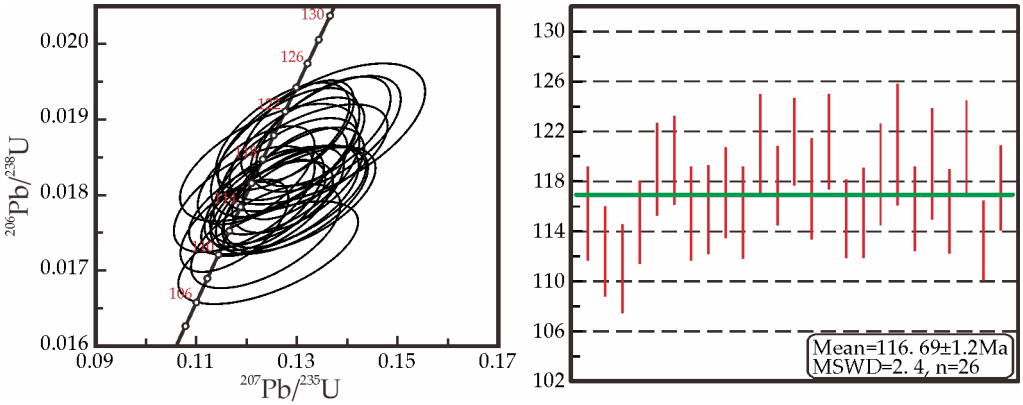


Figure 6. Monazite U-Pb concordia diagrams of the Xidouya gold deposit.

5.4. Pyrite Rb-Sr Ages

Rb-Sr isotopic analysis of eight pyrite samples from the mineralization Stage II (Table 4) shows that the $^{87}Rb/^{86}Sr$ ratios range from 0.7351 to 20.3274, and the measured ($^{87}Sr/^{86}Sr$) ratios vary from 0.711461 to 0.743643, with a good linear relationship observed in the $^{87}Rb/^{86}Sr$ vs. $^{87}Sr/^{86}Sr$ diagram (Figure 7). The isochron age of pyrite calculated using the ISOPLOT 3.0 software [39] is 117.2 ± 3.3 Ma, with an initial $^{87}Sr/^{86}Sr$ ratio of 0.71012 ± 0.00042 (MSWD = 1.02) (Figure 7).

Table 4. The mass fractions and isotope ratios of Rb and Sr in pyrite from the Xidouya gold deposit.

Sample Number	Mineral	Rb (ppm)	Sr (ppm)	$^{87}Rb/^{86}Sr$	Std Err	$(^{87}Sr/^{86}Sr)n$	Std Err
XDY3B1.1	Pyrite	0.544	0.857	1.8357	0.5	0.712693	0.000017
XDY3B1.2	Pyrite	3.418	3.633	2.7226	0.5	0.714535	0.000012
XDY3B1.3	Pyrite	4.511	1.646	7.9315	0.5	0.723537	0.000015
XDY3B1.4	Pyrite	1.607	6.327	0.7351	0.5	0.711461	0.000014
XDY3B1.5	Pyrite	2.057	0.592	10.0568	0.5	0.727021	0.00002
XDY3B1.6	Pyrite	1.003	2.473	1.1734	0.5	0.712018	0.000011
XDY3B1.7	Pyrite	2.922	0.416	20.3274	0.5	0.743643	0.000013
XDY3B1.8	Pyrite	1.758	0.697	7.2987	0.5	0.722192	0.000014

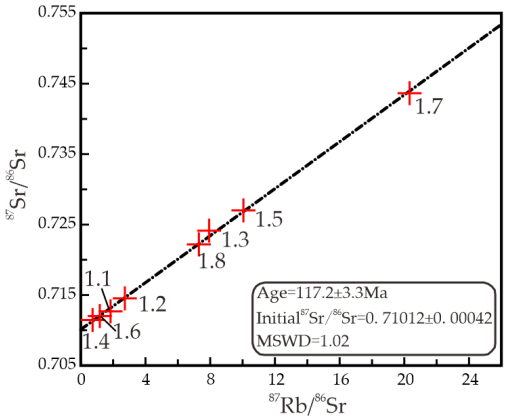


Figure 7. Rb-Sr isotope data and isochron ages of pyrite from the Xidouya gold deposit. The numbers (1.1–1.8) are meaning the sequence no. in Table 4.

6. Discussion

6.1. Mineralization Timing

Precise determination of mineralization timing is the key to understanding deposit genesis and regional metallogenic regularity. This study carries out high-precision monazite U-Pb and pyrite Rb-Sr isotopic dating for the Xidouya gold deposit. The hydrothermal monazite separated from quartz–pyrite ores of the mineralization Stage II yields a weighted mean $^{206}Pb/^{238}U$ age of 116.69 ± 1.2 Ma (MSWD = 2.4). Monazite can crystallize directly from ore-forming fluids in hydrothermal deposits and has a high closure temperature for the U-Pb isotopic system, which can effectively record the precise timing of hydrothermal mineralization activity [51–53]. This age can be reliably interpreted as the main mineralization age of the Xidouya gold deposit.

Pyrite is a ubiquitous and dominant sulfide mineral in hydrothermal gold deposits, typically precipitating synchronously with the main ore-forming processes. During its crystallization from hydrothermal fluids, trace amounts of rubidium (Rb) and strontium (Sr) can be incorporated into the pyrite lattice or trapped within primary fluid inclusions. Because the Rb-Sr isotopic system in pyrite is characterized by a relatively high closure temperature, it strongly resists isotopic resetting from subsequent low-temperature thermal or tectonic events [17,54–57]. Consequently, pyrite Rb-Sr isochron dating has been proven to be a highly reliable and robust method for directly determining the absolute timing of hydrothermal mineralization, accurately reflecting the age of the ore-forming fluid activity [17,54]. The pyrite Rb-Sr isochron age of the same mineralization stage is 117.2 ± 3.3 Ma, with an initial $^{87}Sr/^{86}Sr$ ratio of 0.71012 ± 0.00042 (Figure 7). This age is in good agreement with the monazite U-Pb age within analytical errors, and the two independent isotopic dating methods mutually corroborate each other, precisely constraining the main mineralization age of the Xidouya gold deposit to 117 Ma. This age is highly consistent with the mainstream regional mineralization peak of 120 ± 5 Ma in the Jiaodong gold concentration area [15,18,19,57–59], indicating that the Xidouya gold deposit is a typical product of the large-scale regional gold mineralization event in the Early Cretaceous.

6.2. Ore-Forming Fluid Source

H-O isotopic composition is a powerful and effective geochemical tool for tracing the origin of ore-forming fluids, which has been widely used to constrain the source of ore-forming fluids for various genetic types of mineral deposits [60,61]. In this study, the δD values of ore-forming fluids in different mineralization stages range from −88.0‰ to −75.0‰ with an average of −82.6‰, which falls entirely within the typical δD range of mixed magmatic and meteoric fluids, indicating that the ore-forming fluids are not dominated by metamorphic water (Figure 8). Extensive H-O isotopic studies have been conducted in the Jiaodong gold concentration area by previous researchers, yielding a relatively mature understanding of the H-O isotopic geochemical background of major rocks and fluids in this area. The $\delta^{18}O_{SMOW}$ values of the Jiaodong Group strata range from 5.1‰ to 11.3‰, and the δD values vary from −96‰ to −81‰ [62]. Previous determinations of δD compositions of biotite in Late Jurassic granites and Early Cretaceous granodiorites in the Jiaodong gold concentration area show that the δD ranges of the two rock types are −72 ± 11‰ and −102 ± 15‰ [63], respectively, with corresponding $\delta^{18}O_{SMOW}$ values of < 7‰ and 10.1 ± 0.4‰ [64,65]. Accurate H-O isotopic background values of Mesozoic meteoric water in the Jiaodong gold concentration area have also been obtained by previous geochemical calculations [65,66].

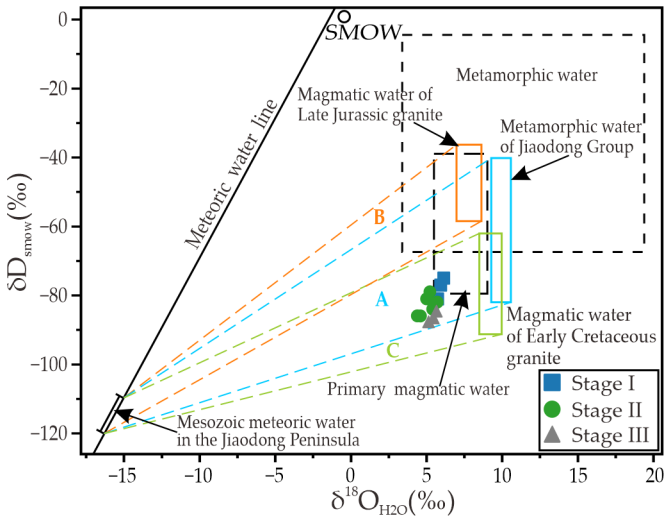


Figure 8. Isotopic compositions of oxygen and hydrogen in the Xidouya gold deposit (modified after [67,68]). Regions A, B, and C represent the mixing areas of meteoric water with metamorphic water of the Jiaodong Group, magmatic water of Late Jurassic granite, and magmatic water of Early Cretaceous granite, respectively.

From the δD-$\delta^{18}O_{H_2O}$ isotopic cross-plot (Figure 8), it can be found that the H-O isotopic compositions of quartz from the Xidouya gold deposit show a good overlap with Zone A (mixed fluid zone of primary magmatic water and meteoric water of the Jiaodong Group) and Zone C (mixed fluid zone of Early Cretaceous primary magmatic water and meteoric water). Previous sampling and dating of granodiorite in the deep part of the Xidouya gold deposit yielded an age of 127.8 ± 1.1 Ma [23], indicating the presence of an Early Cretaceous granite body in the deep part of the deposit. Ore-forming fluids underwent intense water–rock interaction with this granite body during migration and ascent, which significantly affected the geochemical properties of the ore-forming fluids. The average $\delta^{18}O_{H_2O}$ value of the ore-forming fluid in Stage I is 5.9‰, which is close to the characteristic range of magmatic water (5‰–10‰), suggesting the presence of a magmatic water-dominated fluid in the early stage. The average $\delta^{18}O_{H_2O}$ value of Stage II drops to 5.2‰, reflecting an increased incorporation of meteoric water into the fluid system. The average $\delta^{18}O_{H_2O}$ value of Stage III slightly increases, but the δD and $\delta^{18}O_{H_2O}$ values of the ore-forming fluid show an overall decreasing trend with the evolution of mineralization from Stage I to III. While other fluid models cannot be entirely ruled out, these geochemical characteristics are highly compatible with a mixed fluid system that underwent progressive meteoric water influx and fluid–rock interaction during migration.

6.3. Ore-Forming Processes

Sulfur isotope is a core geochemical indicator for tracing the source of ore-forming materials in hydrothermal mineral deposits. The sulfide $\delta^{34}S$ values obtained in this study range from 5.82‰ to 8.63‰ with an average of 7.43‰, showing a narrow and concentrated distribution with a consistent positive deviation from meteoritic sulfur ($\delta^{34}S$ = 0‰), which is highly consistent with the sulfur isotopic characteristics of major geological bodies in the Jiaodong gold concentration area. These geochemical characteristics suggest that the sulfur source of the Xidouya gold deposit is not derived from a single end-member. Instead, the data support a mixed-source hypothesis, predominantly involving anatectic ancient crustal materials with a potential minor contribution of mantle-derived sulfur. The $\delta^{34}S$ values are relatively high in Stage I and distinctly lower in Stage II, and this evolutionary trend is closely related to the regional tectonic stress transition from compression to extension

in the Early Cretaceous (Figure 4). Extensional tectonics provided open pathways for fluid migration and increased the oxidation state of the mineralization environment. This oxidizing environment intensified sulfur isotope fractionation, resulting in $\delta^{34}S$ values that are consistently higher in pyrite than in chalcopyrite. This distinct fractionation pattern strongly indicates a multi-source origin for the ore-forming sulfur. The host rocks of the mining area are Paleoproterozoic metamorphic rocks and Mesozoic granites, and sulfur in these rocks can generate crust-derived sulfur with high $\delta^{34}S$ values through metamorphism and anatexis, providing an important material basis for gold mineralization in the Xidouya deposit.

The initial pyrite Rb-Sr isotopic ratio (0.71012 ± 0.00042) falls between typical mantle (0.703–0.707) and average crustal (0.715–0.720) compositions. While this is consistent with a crust–mantle mixing signature, it is important to note that such isotopic values can also result from the assimilation of highly radiogenic crustal fluids. Based on sulfur and strontium isotopic data, the Xidouya gold deposit is characterized by a typical "crust–mantle mixed" source system. The ore-forming materials were mainly derived from the host monzogranite's source region, which is dominated by melted ancient crust, and later incorporated Early Cretaceous granitic crustal components during fluid ascent.

6.4. Metallogenic Geodynamic Setting

This Early Cretaceous metallogenic event occurred within a well-established regional geodynamic framework characterized by the destruction of the North China Craton. Combined with the regional tectonic evolution background, the North China Craton experienced extensive lithospheric thinning and the establishment of an extensional tectonic regime during the Early Cretaceous (135–110 Ma) [15,69–71]. Before 135 Ma, the Paleo-Pacific Plate subducted slowly toward the northwest. During 135–125 Ma, the subduction direction gradually rotated clockwise and the subduction rate accelerated significantly. After 125 Ma, the sudden break-off and rollback of the subducting Paleo-Pacific Plate triggered a regional tectonic shift from a transpressional to a transtensional regime. This Early Cretaceous transition drove subsequent lithospheric extension, thinning, and asthenospheric upwelling [15,69–71].

These deep-seated processes provided a highly favorable geodynamic setting for large-scale gold mineralization in the Jiaodong concentration area. The mineralization age of the Xidouya gold deposit coincides exactly with the peak of this tectono-magmatic activity, indicating that the formation of the deposit is closely related to mantle partial melting, crustal material anatexis and intense hydrothermal fluid activity induced by lithospheric extension. Its metallogenic dynamic setting is thus controlled by the regional tectono-magmatic events during the destruction of the North China Craton in the Early Cretaceous.

7. Conclusions

Consistent monazite U-Pb and pyrite Rb-Sr isotopic dating precisely constrains the main mineralization age of the Xidouya gold deposit to 117 Ma. This timing perfectly aligns with the regional mineralization peak in the Jiaodong area, indicating the deposit formed during the Early Cretaceous extensional regime triggered by the destruction of the North China Craton.

H-O isotopic compositions suggest that the ore-forming fluids are of mixed magmatic and meteoric origin. The data trace an evolution from a magmatic water-dominated system in the early mineralization stage to a system with an increasing proportion of meteoric water input in the late stage, reflecting a mineralization process characterized by intense water–rock interaction and progressive fluid mixing in an open tectonic system.

Sulfur isotopic compositions indicate that the sulfur source of the ore-forming materials is a mixed product, dominated by crust-derived sulfur with a potential minor mantle input. The initial pyrite Rb-Sr isotopic composition further supports the hypothesis that the ore-forming materials are derived from a typical crust–mantle mixing system, which is likely related to the anatexis of ancient crust and the intense Early Cretaceous magmatic activity in the Jiaodong gold concentration area.

Author Contributions: Conceptualization, F.Z. and J.T.; methodology, J.T.; investigation, F.Z., Z.L., P.G., T.T. and D.L.; resources, Z.L.; data curation, F.Z., B.L., T.T., J.Y. and P.Z.; writing—original draft preparation, F.Z., Z.L., P.G. and T.T.; writing—review and editing, F.Z., Z.L. and J.T.; project administration, J.T.; funding acquisition, J.T. All authors have read and agreed to the published version of the manuscript.

Funding: This research was financially supported by the Shandong Provincial Natural Science Foundation, China (No. ZR2025QC426), the Open Fund of Shandong Engineering Research Center of Underground Resources and Environment High Precision Detection/Shandong Engineering Research Center of Underground Resources and Environment High Precision Detection (No. KY2025005), and the Doctoral Research Foundation of Shandong Jianzhu University (No. X21005Z).

Data Availability Statement: All data are contained within the article.

Conflicts of Interest: The authors declare no conflicts of interest.

References

1. Deng, J.; Wang, Q.F.; Zhang, L.; Xue, S.C.; Liu, X.F.; Yang, L.; Yang, L.Q.; Qiu, K.F.; Liang, Y.Y. Metallogenetic model of Jiaodong-type gold deposits, eastern China. *Sci. China Earth Sci.* **2023**, *66*, 2287–2310. [CrossRef]
2. Yang, L.Q.; Deng, J.; Yang, W.; Xie, D.; Wang, L.; Qiu, K.F.; Li, D.P. Jiaodong-Type Gold Deposit. *Acta Pet. Sin.* **2024**, *40*, 1691–1711. (In Chinese with English Abstract) [CrossRef]
3. Groves, D.I.; Santosh, M.; Deng, J.; Wang, Q.F.; Yang, L.Q.; Zhang, L. A holistic model for the origin of orogenic gold deposits and its implications for exploration. *Min. Depos.* **2020**, *55*, 275–292. [CrossRef]
4. Song, M.C.; Li, J.; Dong, L.L.; Li, J.; Bai, X.; Hu, W.X. Where does the enormous gold endowment in the Jiaodong Peninsula originate from? *Gondwana Res.* **2026**, *154*, 188–200. [CrossRef]
5. Fan, H.R.; Feng, K.; Li, X.H.; Hu, F.F.; Yang, K.F. Mesozoic gold mineralization in the Jiaodong and Korean peninsulas. *Acta Pet. Sin.* **2016**, *32*, 3225–3238. (In Chinese)
6. Song, M.C.; Song, Y.X.; Ding, Z.Z.; Li, S.Y. Jiaodong Gold Deposits: Essential Characteristics and Major Controversy. *Gold Sci. Technol.* **2018**, *26*, 406–422. (In Chinese with English Abstract)
7. Liu, Q.; Zhang, Y.; Cai, N.; Zhang, C.; Li, D.P.; Sui, H.J.; Wei, P.F.; Geng, K.; Xie, W. Analysis on Geological Characteristics and Resource Potential of Hushan-Xidouya Gold Deposit in Qixia City in Shandong Province. *Shandong Land Resour.* **2024**, *40*, 33–41. (In Chinese with English Abstract)
8. Cao, T.S.; Shi, H.J.; Kang, G.M.; Zhao, Y.B.; Zhang, J.K.; Tian, S.B.; Zhao, E.F. *Detailed Investigation Report on the Gold Deposit in Ore Belt No. I, Xidouya Mining Area, Qixia City, Shandong Province*; Yantai Jinman Investment Co., Ltd.: Yantai, China, 2012; pp. 1–69. (In Chinese)
9. Goldfarb, R.J.; Santosh, M. The dilemma of the Jiaodong gold deposits: Are they unique? *Geosci. Front.* **2014**, *5*, 139–153. [CrossRef]
10. Santiago, T.; José, M.G.-J.; Martin, R.; Manuel, E.S.; Diego, M.; Graham, B.; Edward, S.; William, L.G.; Suzanne, Y.O.R.; Michel, G.; et al. Plume-subduction interaction forms large auriferous provinces. *Nat. Commun.* **2017**, *843*, 843. [CrossRef]
11. Wang, Z.C.; Cheng, H.; Zong, K.Q.; Geng, X.L.; Wang, C.Y. Metasomatized lithospheric mantle for Mesozoic giant gold deposits in the North China craton. *Geology* **2019**, *48*, 169–173. [CrossRef]
12. Deng, J.; Wang, Q.F.; Santosh, M.; Liu, X.F.; Yang, L. Remobilization of metasomatized mantle lithosphere: A new model for the Jiaodong gold province, eastern China. *Miner. Depos.* **2020**, *55*, 257–274. [CrossRef]
13. Jiang, Y.H.; Du, F.G.; Qing, L.; Ni, C.Y. Elemental and multiple isotopic evidences of enriched lithospheric mantle origin of the Xiadian gold deposit in the Jiaodong Peninsula, East China. *Ore Geol. Rev.* **2020**, *127*, 103824. [CrossRef]
14. Fan, Y.C. *Origins of Ore-Forming Materials and the Metallogenic Model of Gold Deposits in the Jiaoxibei Area*; Jilin University: Jilin, China, 2022.
15. Deng, J.; Yang, L.Q.; Groves, D.I.; Zhang, L.; Qiu, K.F.; Wang, Q.F. An integrated mineral system model for the gold deposits of the giant Jiaodong province, eastern China. *Earth-Sci. Rev.* **2020**, *208*, 103274. [CrossRef]

16. Li, J.J.; Luo, Z.K.; Liu, X.Y.; Xu, W.D.; Luo, H. Geodynamic setting for formation of large-superlarge gold deposits and Mesozoic granites in Jiaodong area. *Miner. Depos.* **2005**, *24*, 361–372. (In Chinese)
17. Yang, J.H.; Zhou, X.H. Rb-Sr, Sm-Nd, and Pb isotope systematics of pyrite: Implications for the age and genesis of lode gold deposits. *Geology* **2001**, *29*, 711–714. [CrossRef]
18. Zhang, L.; Weinberg, R.F.; Yang, L.Q.; Groves, D.I.; Sai, S.X.; Matchan, E.; Phillips, D.; Kohn, B.P.; Miggins, D.P.; Liu, Y.; et al. Mesozoic Orogenic Gold Mineralization in the Jiaodong Peninsula, China: A Focused Event at 120±2 Ma During Cooling of Pregold Granite Intrusions. *Econ. Geol.* **2020**, *115*, 415–441. [CrossRef]
19. Li, J.J.; Dang, Z.C.; Fu, C.; Zhang, P.P.; Tian, J.P.; He, J.T. Genesis of the Yangjiakuang gold deposit, Jiaodong peninsula, China: Constraints from S-He-Ar-Pb isotopes, and Sm-Nd and U-Pb geochronology. *Front Earth Sci.* **2023**, *11*, 1048509. [CrossRef]
20. Wang, M.Y.; Li, J.; Song, M.; Zhang, L.P.; Tang, Z.Y.; Ding, Z.J. The metallogenic mechanism of the Dadengge gold polymetallic deposit in the Jiaodong Peninsula: Constraints from pyrite Rb-Sr dating, in situ S isotope and trace elements. *Acta Pet. Sin.* **2023**, *39*, 1501–1515. (In Chinese with English Abstract) [CrossRef]
21. Liao, M.W.; Chen, Y.H.; Xie, J.M. Geological Characteritics and Deep Gold Prospecting of Hushan-Xidouya Gold Deposit in Qixia City of Shandong Province. *Shandong Land Resour.* **2014**, *30*, 21–26. (In Chinese with English Abstract)
22. Xie, J.M.; Xiao, X.; Liu, P.; Shi, H.J.; Cui, Y.F. Geological Characteristics and Exploration Direction of Xidouya Deposit in Qixia City of Shandong Province. *Shandong Land Resour.* **2011**, *27*, 1–5. (In Chinese with English Abstract)
23. Tian, J.P. *The Mesozoic Gold Polymetallic Regional Metallogeny in Qipengfu Ore Concentration Area, Jiaodong Peninsula*; China University of Geosciences: Beijing, China, 2020.
24. Tian, R.C. *Geochemistry of Mineralization in the Penglai-Qixia Gold Belt, Jiaodong Peninsula*; China University of Geosciences: Beijing, China, 2022.
25. He, J.T.; Li, J.J.; Shi, G.Y.; Wang, C.G.; Man, R.H. Genetic mineralogy and geological significance of pyrites from the Muping-Rushan Gold Belt, Jiaodong Peninsula. *Geoscience* **2025**, *39*, 667–680. (In Chinese with English Abstract) [CrossRef]
26. Yu, G.P.; Xu, T.; Ai, Y.S.; Chen, L.; Yang, J.H. Significance of crustal extension and magmatism to gold deposits beneath Jiaodong Peninsula, eastern North China Craton: Seismic evidence from receiver function imaging with a dense array. *Tectonophysics* **2020**, *789*, 228532. [CrossRef]
27. Zheng, Y.F.; Zhao, Z.F.; Chen, R.X. Ultrahigh-pressure metamorphic rocks in the Dabie–Sulu orogenic belt: Compositional inheritance and metamorphic modification. *Geol. Soc. Lond. Spec. Publ.* **2019**, *474*, 89–132. [CrossRef]
28. Song, M.C.; Lin, S.Y.; Yang, L.Q.; Song, Y.X.; Ding, Z.J.; Li, J.; Li, S.Y.; Zhou, M.L. Metallogenic model of Jiaodong Peninsula gold deposits. *Miner. Depos.* **2020**, *39*, 215–236.
29. Fan, H.R.; Lan, T.G.; Li, X.H.; Santosh, M.; Yang, K.F.; Hu, F.F.; Feng, K.; Hu, H.L.; Peng, H.W.; Zhang, Y.W. Conditions and Processes Leading to Large-Scale Gold Deposition in the Jiaodong Province, Eastern China. *Sci. China Earth Sci.* **2021**, *64*, 1504–1523. (In Chinese with English Abstract) [CrossRef]
30. Liu, Z.J.; Cheng, S.B.; Liu, C.R.; Gu, B.J.; Xue, Y.S. Geochronology and Genesis of the Shuigou Gold Deposit, Qixia-Penglai-Fushan Metallogenic Area, Jiaodong Peninsula, Eastern China: Constraints from SHRIMP U-Pb, 40Ar/39Ar Age, and He-Ar Isotopes. *Minerals* **2025**, *15*, 14. [CrossRef]
31. Tian, J.P.; Wang, J.H.; Wang, L.M.; Ren, T.L.; Wang, L.G.; Zhang, W.; Sun, B.; Yu, X.W.; Wang, Y.P.; Guo, Y.; et al. Formation age and genesis of the Hushan gold deposit, Jiaodong Peninsula, North China: Monazite chronological and geochemical evidence. *Earth Sci. Front.* **2026**, *33*, 163–180. (In Chinese with English Abstract)
32. He, J.T.; Li, J.J.; Liu, L.L.; Tian, J.P.; Man, R.H.; Shi, G.Y.; Wang, C.G.; Feng, Z. Geological and S–Pb–He–Ar isotope constraints on the origin of the Muping–Rushan gold belt, Jiaodong Peninsula, eastern China. *BSGF Earth Sci. Bull.* **2025**, *196*, 9. [CrossRef]
33. Clayton, R.; Mayeda, T. The use of bromine pentafluoride in the extraction of oxygen from oxides and silicates for isotopic analysis. *Geochim. Cosmochim. Acta* **1963**, *27*, 43–52. [CrossRef]
34. Coleman, M.L.; Shepherd, T.J.; Durham, J.J.; Rouse, J.E.; Moore, G.R. Reduction of water with zinc for hydrogen isotope analysis. *Anal. Chem.* **1982**, *54*, 993–995. [CrossRef]
35. Cui, Y.R.; Zhou, H.Y.; Geng, J.Z.; Li, H.K.; Li, H.M. In Situ LA-MC-ICP-MS U-Pb Isotopic Dating of Monazite. *Acta Geosci. Sin.* **2012**, *33*, 865–876.
36. Tu, J.R.; Cui, Y.R.; Zhou, H.Y.; Li, H.M.; Hao, S.; Li, G.Z. Review of U-Pb dating methods for cassiterite. *Geol. Surv. Res.* **2019**, *42*, 241–249. (In Chinese with English Abstract)
37. Liu, Y.S.; Hu, Z.C.; Zong, K.Q.; Gao, C.G.; Gao, S.; Xu, J.A.; Chen, H.H. Reappraisement and refinement of zircon U-Pb isotope and trace element analyses by LA-ICP-MS. *Chin. Sci. Bull.* **2010**, *55*, 1535–1546. [CrossRef]
38. Ludwig, K.R. User's manual for isoplot 3.75, A geochronological toolkit for Microsoft Excel. *Berkeley Geochronol. Cent. Spec. Publ.* **2012**, *5*, 1–75.
39. Ludwig, K.R. *Isoplot 3.00: A Geochronological Toolkit for Microsoft Excel*; Special Publications 4; Berkeley Geochronology Center: Berkeley, CA, USA, 2003; pp. 70–72. Available online: https://searchworks.stanford.edu/view/6739593 (accessed on 18 March 2026).

40. Liu, W.G.; Liu, H.B.; Li, G.Z.; Xiao, Z.B.; Tu, J.R.; Li, H.M. The Application of Ion Exchange Resins in Sr-Nd Isotopic Assay of Geological Samples. *Acta Geol. Sin.* **2017**, *91*, 2584–2592. (In Chinese)
41. Clayton, R.N.; O'Neil, J.R.; Mayeda, T.K. Oxygen isotope exchange between quartz and water. *J. Geophys. Res.* **1972**, *77*, 3057–3067. [CrossRef]
42. Huang, D.Y. Sulfur isotope studies of the metallogenic series of gold deposits in Jiaodong area. *Miner. Depos.* **1994**, *13*, 75–86. (In Chinese)
43. Wang, Y.W.; Zhu, F.S.; Gong, R.T. Tectonic isotope geochemistry-Further study on sulphur isotope of Jiaodong Gold Concentration Area. *Gold* **2002**, *23*, 1–16. (In Chinese)
44. Deng, J.; Wang, C.M.; Bagas, L.; Carranza, E.J.M.; Lu, Y.J. Cretaceous–Cenozoic tectonic history of the Jiaojia Fault and gold mineralization in the Jiaodong Peninsula, China: Constraints from zircon U–Pb, illite K–Ar, and apatite fission track thermochronometry. *Min. Depos.* **2015**, *50*, 987–1006. [CrossRef]
45. Zhang, Z.R.; Cheng, S.Z. Superlarge gold deposit exploration perspective in Jiaolai Basin of Jiaodong gold metallogenetic domain. *Geochimica* **1999**, *28*, 203–212. (In Chinese with English Abstract)
46. Li, Z.L.; Yang, M.Z. *The Geology-Geochemistry of Gold Deposits in Jiaodong Region*; Tianjin Science and Technology Press: Tianjin, China, 1993; pp. 1–300. (In Chinese)
47. Xu, J.F. The Age and Petrological Characteristics of the Kunyushan Rock. *Shandong Geol. Intell.* **1986**, *2*, 24–37. (In Chinese with English Abstract)
48. Yang, Z.F.; Xu, J.K.; Zhao, L.S.; Shen, Y.L.; Wu, Y.B. *Regional Crust Evolution and Geochemistry of Gold Mineralization in Jiaodong*; Geological Publishing House: Beijing, China, 1998; pp. 1–157. (In Chinese)
49. Zi, J.W.; Muhling, J.R.; Rasmussen, B. Geochemistry of low-temperature (<350 °C) metamorphic and hydrothermal monazite. *Earth-Sci. Rev.* **2024**, *249*, 104668. [CrossRef]
50. Liang, X.; Xu, Y.J.; Zi, J.W.; Zhang, H.C.; Du, Y.S. Genetic Mineralogy of Monazite and Constraints on Interpretation of U-Th-Pb Ages. *Earth Sci.* **2022**, *47*, 1383–1398. (In Chinese with English Abstract) [CrossRef]
51. Franck, P.; Simon, C.; Thomas, S. Electron microprobe and LA-ICP-MS study of monazite hydrothermal alteration:: Implications for U-Th-Pb geochronology and nuclear ceramics. *Geochim. Cosmochim. Acta* **2000**, *64*, 3283–3297. [CrossRef]
52. Harlaux, M.; Mercadier, J.; Marignac, C.; Peiffert, C.; Cloquet, C.; Cuney, M. Tracing metal sources in peribatholitic hydrothermal W deposits based on the chemical composition of wolframite: The example of the Variscan French Massif Central. *Chem. Geol.* **2018**, *479*, 58–85. [CrossRef]
53. Seydoux-Guillaume, A.-M.; Wirth, R.; Deutsch, A.; Schärer, U. Microstructure of 24-1928 Ma concordant monazites; implications for geochronology and nuclear waste deposits. *Geochim. Cosmochim. Acta* **2004**, *68*, 2517–2527. [CrossRef]
54. Li, Q.L.; Chen, F.K.; Yang, J.H.; Fan, H.R. Single grain pyrite Rb–Sr dating of the Linglong gold deposit, eastern China. *Ore Geol. Rev.* **2008**, *34*, 263–270. [CrossRef]
55. Hu, Q.Q.; Wang, Y.T.; Chen, S.C.; Wei, R.; Liu, X.L.; Liu, J.C.; Wang, R.T.; Gao, W.H.; Wang, C.A.; Tang, M.J.; et al. Genesis of the Dongtangzi Zn-Pb Deposit of the Fengxian–Taibai Ore Cluster in West Qinling, China: Constraints from Rb-Sr and Sm-Nd Geochronology, and In Situ S-Pb Isotopes. *Minerals.* **2024**, *14*, 297. [CrossRef]
56. Xu, L.; Yang, J.H.; Zeng, Q.D.; Xie, L.W.; Zhu, Y.S.; Li, R.; Li, B. Pyrite Rb-Sr, Sm-Nd and Fe isotopic constraints on the age and genesis of the Qingchengzi Pb-Zn deposits, northeastern China. *Ore Geol Rev.* **2020**, *117*, 103324. [CrossRef]
57. Tian, J.P.; Wang, J.H.; Tian, T.L.; Wang, L.G.; Wang, Y.P.; Yu, X.W.; Zhang, W.; Ren, T.L.; Sun, B. In-Situ Geochemical and Rb–Sr Dating Analysis of Sulfides from a Gold Deposit Offshore of Northern Sanshandao, Jiaodong Peninsula, North China: Implications for Gold Mineralization. *Minerals* **2024**, *14*, 456. [CrossRef]
58. Deng, J.; Qiu, K.F.; Wang, Q.F.; Goldfarb, R.; Yang, L.Q.; Zi, J.W.; Geng, J.Z.; Ma, Y. In Situ Dating of Hydrothermal Monazite and Implications for the Geodynamic Controls on Ore Formation in the Jiaodong Gold Province, Eastern China. *Econ. Geol.* **2020**, *115*, 671–685. [CrossRef]
59. Li, J.W.; Vasconcelos, P.M.; Zhang, J.; Zhou, M.F.; Zhang, X.J.; Yang, F.H. 40Ar/39Ar constraints on a temporal link between gold mineralization, magmatism, and continental margin transtension in the Jiaodong Gold Province, eastern China. *J. Geol.* **2003**, *111*, 741–751. [CrossRef]
60. Qiu, K.F.; Taylor, R.D.; Song, Y.H.; Yu, H.C.; Song, K.R.; Li, N. Geologic and geochemical insights into the formation of the Taiyangshan porphyry copper–molybdenum deposit, Western Qinling Orogenic Belt, China. *Gondwana Res.* **2016**, *35*, 40–58. [CrossRef]
61. Qiu, K.F.; Marsh, E.; Yu, H.C.; Pfaff, K.; Gulbransen, C.; Gou, Z.Y.; Li, N. Fluid and metal sources of the Wenquan porphyry molybdenum deposit, Western Qinling, NW China. *Ore Geol. Rev.* **2017**, *86*, 459–473. [CrossRef]
62. Chen, Z.S.; Zhang, L.G.; Liu, J.X.; Wang, B.C.; Xu, J.F.; Zheng, W.S. A Preliminary Study on Hydrogen and Oxygen Isotope Geochemical Backgrounds of Geological Bodies in Jiaodong (Eastern Shandong) Gold Metallogenic Region. *Acta Petrol. Mineral.* **1995**, *14*, 211–218. (In Chinese with English Abstract)

63. Mao, J.W.; Li, H.M.; Wang, Y.T.; Zhang, C.Q.; Wang, R.T. The relationship between mantle-drived fluid gold ore-formation in the eastern Shandong peninsula: Evidences from D-O-C-S isotopes. *Acta Pet. Sin.* **2005**, *79*, 839–857. (In Chinese)
64. Lin, W.W.; Yin, X.L. Isotope Geological Characteristics of Mineralizing Fluids of Gold Deposits in Jiaodong Area and a Discussion on the Application Conditions of H. P. Taylor's Equation. *Acta Petrrologica Mineral.* **1998**, *17*, 249–259. (In Chinese with English Abstract)
65. Zhang, L.G.; Chen, Z.S.; Liu, J.X. Water-rock exchange in the Jiaojia type gold deposit: A study of hydrogen and oxygen isotopic composition of ore-forming fluids. *Miner. Depos.* **1994**, *13*, 193–200. (In Chinese with English Abstract)
66. Craig, H. Isotopic variations in meteoric waters. *Science* **1961**, *133*, 1702–1703. [CrossRef] [PubMed]
67. Guo, L.N.; Zhang, C.; Song, Y.Z.; Chen, B.H.; Wang, Y.W. Hydrogen and oxygen isotopes geochemistry of the Wang' ershan gold deposit, Jiaodong. *Acta Pet. Sin.* **2014**, *30*, 2481–2494. (In Chinese with English Abstract)
68. Wang, L.G.; Yang, L.Q.; Yang, W.; Zhi, Y.B.; Xie, D.; Sun, B.; Zhang, W.; Li, X.Z.; Wang, Y.P.; Wang, J.H. Genesis and exploration potential of gold deposits in Archean high-amphibolite facies metamorphic rocks of the Jiaodong Peninsula: Geological and geochemical constraints from the Majiayao gold deposit. *Ore Geol. Rev.* **2025**, *181*, 106596. [CrossRef]
69. Zhai, M.G.; Fan, H.R.; Yang, J.H.; Miao, L.C. Large-scale cluster of gold deposits in east shandong: Anorogenic metallogenes. *Earth Sci. Front.* **2004**, *11*, 85–98. (In Chinese with English Abstract)
70. Sun, W.D.; Ding, X.; Hu, Y.H.; Li, X.H. The golden transformation of the Cretaceous plate subduction in the west Pacific. *Earth Planet. Sci. Lett.* **2007**, *262*, 533–542. [CrossRef]
71. Zhu, R.X.; Chen, L.; Wu, F.Y.; Liu, J.L. Timing, scale and mechanism of the destruction of the North China Craton. *Sci. China Earth Sci.* **2011**, *547*, 89–97. [CrossRef]

Disclaimer/Publisher's Note: The statements, opinions and data contained in all publications are solely those of the individual author(s) and contributor(s) and not of MDPI and/or the editor(s). MDPI and/or the editor(s) disclaim responsibility for any injury to people or property resulting from any ideas, methods, instructions or products referred to in the content.